

Controlled Synthesis of Perforated Oxide Nanosheets with High Density Nanopores Showing Superior Water Purification Performance

Yongtao Li,[#] José Julio Gutiérrez Moreno,[#] Zhaoqi Song, Dongqing Liu, Maoyu Wang, Aymeric Ramiere, Zhenxing Feng, Qingshan Jason Niu, Takayoshi Sasaki, and Xingke Cai*



Cite This: *ACS Appl. Mater. Interfaces* 2022, 14, 18513–18524



Read Online

ACCESS |



Metrics & More



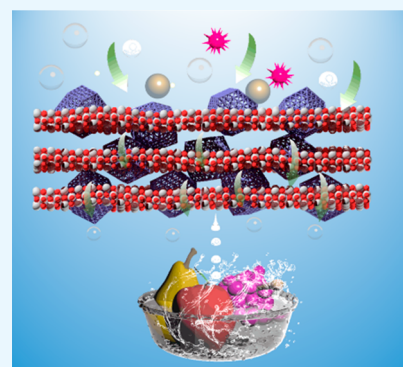
Article Recommendations



Supporting Information

ABSTRACT: A method for creating genuine nanopores in high area density on monolayer two-dimensional (2D) metallic oxides has been developed. By use of the strong reduction capability of hydroiodic acid, active metal ions, such as Fe^{III} and Co^{III}, in 2D oxide nanosheets can be reduced to a divalent charge state (2+). The selective removal of FeO₂ and CoO₂ metal oxide units from the framework can be tuned to produce pores in a range of 1–4 nm. By monitoring of the redox reaction kinetics, the pore area density can be also tuned from $\sim 0.9 \times 10^4$ to $\sim 3.3 \times 10^5 \mu\text{m}^{-2}$. The universality of this method to produce much smaller pores and higher area density than the previously reported ones has been proven in different oxide nanosheets. To demonstrate their potential applications, ultrasmall metal organic framework particles were grown inside the pores of perforated titania oxide nanosheets. The optimized hybrid film showed $\sim 100\%$ rejection of methylene blue (MB) from the water. Its water permeance reached $4260 \text{ L m}^{-2} \text{ h}^{-1} \text{ bar}^{-1}$, which is 1–3 orders of that for reported 2D membranes with good MB rejections.

KEYWORDS: oxide nanosheets, perforated structure, selective etching, assembly, water purification



INTRODUCTION

Fresh water is the most important resource necessary to human life and the life of many other species. Considering that only 1.3% of the fresh water is at the surface and directly accessible to sustain lives, we realize how rare and precious this resource is.¹ However, human activities, with pollution especially, are threatening the scarce fresh water available. The development of water purification technologies to filter out pollutants, both organic and inorganic, and obtain fresh water has become a global priority as the United Nations have listed it as one of the 17 sustainable goals for 2030.² In this context, two-dimensional (2D) nanomaterials, such as graphene, graphene oxides (GO) and MXenes, have emerged as one of the most promising classes of materials to purify water because of their optimum active surface, good mechanical flexibility, and easy fabrication into films/membranes.^{3,4} However, in their restacked films, each nanosheet is tightly attached to each other due to their strong van der Waals forces.⁵ The water molecules can only pass through the film along the edges and narrow interlayers among the sheets, leading to a rather long water pathway and very small water permeance through the 2D films/membranes.⁶ In the meantime, the nanochannels in the film are easy to be blocked by the pollutants and show poor cycling stability.

To overcome these challenges, many strategies have been developed to enhance the water permeance and the cycling

stability by expanding the interlayers of 2D films, such as intercalating polyelectrolytes with the interlayers,^{7–11} hybridizing the 2D films with 1D carbon nanotubes,¹² and opening the sheet edges with metal organic framework (MOF) nanoparticles.¹³ However, the water permeance is still low in such films despite their good selectivity to remove the organic pollutants/salts from the water.

Given the small thickness of the 2D films/membranes, we identify that the best way to enhance the water permeance is to shorten the water pathway through them. If we can make holes on the 2D materials, the water molecules do not have to pass along the interlayers of the films but directly pass each nanosheet through the holes on them. We can predict the great water permeance in the perforated 2D materials assembled films/membranes. Noteworthy, these holes should only allow the water molecules to pass through them but reject the pollutants/salts. In this case, the good selectivity in these films can be retained during the cycling process. Therefore, the holes

Received: January 25, 2022

Accepted: March 31, 2022

Published: April 18, 2022



fabricated on each nanosheet should be in large area density and ultrasmall sizes.

A few works reported the synthesis of perforated 2D materials with thickness of >5 nm by bottom-up strategies, such as BN,¹⁴ black phosphorus,¹⁵ carbon nitrides,¹⁶ carbon nanosheets,¹⁷ and metal oxides.¹⁸ However, such materials are difficult to produce at a large scale and do not have a layered structure, but they are composed of nanoparticles.¹⁹ Thus, the advantages of 2D structures, such as their restacking into an integrated film and good mechanical flexibility, cannot be achieved by these perforated materials. Producing nanopores on monolayer 2D materials should be an ideal choice to merge the advantages of porous and 2D structures. Although defects are commonly found in most monolayer 2D materials, surfaces with a large concentration of pores are rarely reported^{20–22} due to the structural instability of highly defective structures. Some papers reported the fabrication of nanopores on various single monolayer 2D films or nanosheets by electron/ion beam irradiation and nanoparticle assisted photochemical process, which have been used for DNA sequencing.^{23,24} However, these methods are not suitable for synthesizing perforated monolayer nanosheets at a large scale, which are not suitable for the water purification applications.

So far, only a few monolayer 2D materials have been successfully fabricated into perforated structures at a large scale. Pores were produced on graphene oxide (GO) due to the strong chemical reaction between the oxidative functional groups and the reductants at high temperatures. The as-produced perforated reduced GO (rGO) with genuine nanopore sizes from 0.6 to 5 nm showed an electrochemical capacitance up to 200 F g^{-1} , which was much higher than the other reported capacities for rGO.²⁵ As another example, the perforated monolayer MoS₂ was obtained by intercalating the bulk MoS₂ in a lithium-containing liquid ammonia medium and exfoliating them in water. Due to the strong reduction capability of lithium to remove S atoms from the 2D structure, perforated 2D MoS₂ with irregular pores have been obtained.²⁵ MXene has also been fabricated into a perforated structure with >20 nm pores, produced by oxidizing the surface to produce metal oxides and selectively remove them.²⁶ Apparently, these reported scalable production methods cannot precisely control the pore size and density in the perforated monolayer 2D materials. For water purification, the requirements on the pore size are much more restricted.²⁶ Unfortunately, we currently lack a scalable method to produce perforated monolayer 2D materials with genuine and ultrasmall pores.

On the basis of the reported scalable methods, the selective etching strategy by reductants or oxidants seems to be the most suitable method to create pores on the 2D materials on a large scale. To prepare homogeneously distributed ultrasmall pores on 2D materials, a suitable redox mediator and 2D materials must be chosen to ensure the etching can genuinely happen at the molecular scale but would not dissolve the 2D nanosheets. This requires the reaction condition to be relatively mild, having ample space to tune the parameters to control the pore structure finely. Previous research indicated the hydroiodic acid (HI) was a good reductant toward carbon oxides, such as organic α -diketones and α -ketols.^{27,28} During the reduction process, the protons (H^+) in the HI acid coordinated with the oxygen atoms from the oxide, and the iodine ions (I^-) reduced the carbon atoms bonded to oxygens. Recently, HI acid has been successfully used to reduce the GO

and remove the oxygen functional groups on their surface at ambient conditions.²⁹ On the basis of the electrochemical potential of the metal ions and I^- , there is a chance for using the HI acid to reduce some active metal ions inside metal oxides and remove them from the crystals.³⁰

In this work, we used the HI acid to selectively remove the active metal containing units, such as FeO₂ and CoO₂, from titanium-based oxide nanosheets. The active metal dopants (Fe, Co) are distributed throughout the whole titanium oxide-based nanosheet, resulting in genuinely distributed nanopores forming on them. By tuning the acid concentration, the average size of the nanopores on the 2D metallic oxides can be regulated from 1 to 4 nm. These perforated nanosheets were used to grow ultrasmall zeolitic imidazolate framework-8 (ZIF-8) inside the pores, and the as formed hybrid material showed high selectivity to remove organic pollutants at high water permeance.

EXPERIMENTAL SECTION

Synthesis of Metallic Oxide Nanosheets. The synthesis of Ti_{1-x}Fe_xO₂ ($x = 0, 0.1, 0.2, 0.3, 0.4$), Ti_{0.75}Fe_{0.1}Co_{0.15}O₂, and Mn_{0.7}Co_{0.3}O₂ was based on the proton exchange method.^{31–33} Initially, the alkaline metal containing layered precursors were synthesized by solid state calcination. Then, the alkaline metal ions within the interlayers of the precursors were exchanged with protons by the hydrochloride (HCl) acid (1 mol/L). Finally, the protonated precursors were exfoliated into nanosheets by shaking them in the tetrabutylammonium hydroxide (TBAOH) solution for 1 week.

Acid Treatment of Metallic Oxide Nanosheets. 10 mL of metallic oxide nanosheets (2 mg/mL) solution was slowly dropped into 10 mL of acid solution with different concentrations (0.03, 0.05, 0.1, 0.2, 0.3, 0.6, 1.2, and 3 mol/L). After stirring for 10 min, they were centrifuged to separate the I₂ adsorbed oxide nanosheets with the solution. The sediments were washed by hot methanol (50 °C) and centrifuged at 3000 rpm for 10 min to collect the defective metallic oxide nanosheets sediments. The sediments were re-dispersed in the TBAOH solution to get a stable nanosheet suspension for further characterization.

In Situ Growth of ZIF-8 Nanoparticles on the H-Ti_{0.6}Fe_{0.4}O₂ Nanosheets. 20 mg of 2-methylimidazole was dissolved into 60 mL of methanol solution under stirring. Then 10 mL of H-Ti_{0.6}Fe_{0.4}O₂ nanosheets methanol solution at a concentration of 2 mg/mL was slowly added into the 2-methylimidazole solution. Finally, 20 mL of Zn(NO₃)₂·6H₂O methanol solution at a concentration of 0.9 mg/mL was quickly added into the mixed solution under stirring. After different growth periods (30 s, 1 min, and 5 min), 2 mL of mixed solution was immediately taken out and dropped into 40 mL of ethanol solution for fabricating films.

Fabrication of the Films and Their Water Purification Property Measurements. The original Ti_{0.6}Fe_{0.4}O₂, H-Ti_{0.6}Fe_{0.4}O₂, and H-Ti_{0.6}Fe_{0.4}O₂/ZIF-8 solutions were vacuum filtered to form the oxide nanosheet films on the hydrophilic cellulose membranes with pore size of 0.22 μm . Around 0.5 mg of nanosheets was diluted into 40 mL and then filtered to form a film. To check the purification capability, 200 mL of methylene blue (5 mg/L) was filtered by the as fabricated films each time.

Characterization. The size and thickness of the original and defects-rich oxide nanosheets were characterized by atomic force microscopy (Bruker-Innova). The UV-visible absorption spectrometer (Agilent Cary 5000, USA) and inductive coupled plasma emission spectrometer (ICP, MDTC-EQ-M29-01) were used to monitor the change of metallic elements in the oxide nanosheets after the acid treatment. Transmission electron microscopy (TEM, FEI Tecnai G² F30, USA) was used to characterize the morphology and microstructures of the H-Ti_{0.6}Fe_{0.4}O₂ nanosheets and the ZIF-8 grown ones. X-ray photoelectron spectroscopy (XPS, monochromatic Al K α X-rays, PHI Versa Probe II, Japan) and X-ray absorption near edge structure measurement (XANES, APS, USA) were used to

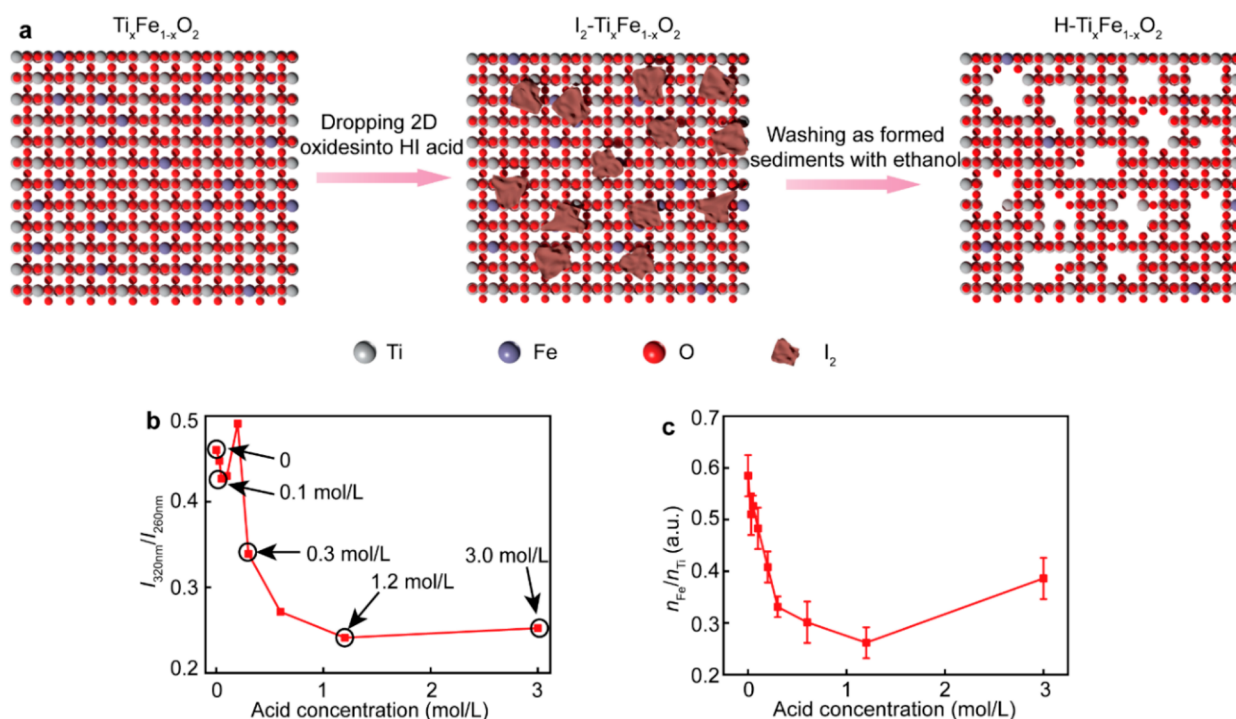


Figure 1. Procedures to create nanopores and composition change characterization: (a) schematic illustration of the procedure to synthesize H-Ti_{0.6}Fe_{0.4}O₂. (b, c) Concentration ratio evolution of Fe^{III} to Ti^{IV} based on their absorbance and ICP results.

examine the structural change of the Fe and Ti after the formation of I₂ on the Ti_{0.6}Fe_{0.4}O₂ surface and the removal of them to form H-Ti_{0.6}Fe_{0.4}O₂. Extended X-ray absorption fine structure (EXAFS) was used to identify the bond structure difference between Ti_{0.6}Fe_{0.4}O₂ and H-Ti_{0.6}Fe_{0.4}O₂. Powder X-ray diffraction (XRD, with monochromatic Cu K α radiation $\lambda = 0.15418$ nm, Bruker D8 Advance, Germany) was used to characterize the layered structure of the as fabricated H-Ti_{0.6}Fe_{0.4}O₂ films and ZIF-8 grown H-Ti_{0.6}Fe_{0.4}O₂ films. Scanning electron microscopy (SEM, Hitachi SU8010, 15 kV, Japan) was used to characterize the cross section of the as fabricated films. The UV-visible absorption spectrometer has also been used to monitor the purification effect of the H-Ti_{0.6}Fe_{0.4}O₂ films by filtering them with the organic pollutants containing water solution.

DFT Calculations. Periodic DFT calculations were carried out within the framework of the Vienna Ab initio Simulation Package (VASP). The projector augmented-wave (PAW) potentials^{34,35} were used to describe the core-valence interaction, with the valence electrons described by periodic plane waves with cutoff energy of 520 eV. We used the generalized gradient approximation (GGA) for the exchange-correlation function as formulated by Perdew and Wang (PW91).³⁶ The convergence criteria used for energy and forces on each atom was 10⁻⁴ eV and 0.02 eV/Å. All the calculations in this study included a correction for on-site Coulomb interactions (DFT +U),³⁷ with $U = 4.5$ eV applied on the Ti 3d electrons and $U = 5.0$ eV applied on the Fe 3d electrons. This correction was applied to account for the potential charge transfer in Ti and Fe atoms that can form in the Ti_{1-x}Fe_xO₂ nanosheet. The U values were chosen based on our previous works on TiO₂ surfaces³⁸⁻⁴¹ and available literature on molecular adsorption at Fe₂O₃.⁴² More details about the computational setup and simulated models are given in the Supporting Information.

RESULTS AND DISCUSSION

Pristine Ti_{1-x}Fe_xO₂ Nanosheets. First, we synthesized pristine Ti_{1-x}Fe_xO₂ ($x = 0, 0.1, 0.2, 0.3, 0.4$) metallic oxide nanosheets using the proton exchange method (see methods). Pristine Ti_{0.6}Fe_{0.4}O₂ nanosheets are examined here for reference. Atomic force microscopy (AFM) characterization

showed the successful preparation of monolayer Ti_{0.6}Fe_{0.4}O₂ nanosheets with a thickness of 1.5 nm and sizes of several micrometers (Figure S1a). We note that our thickness was slightly larger than the previously reported value at 1.2 nm, which we ascribed to the presence of dimethyl sulfoxide (DMSO) solvents between the sheets and the substrates.⁴³ The Fe-doped Ti_{0.6}Fe_{0.4}O₂ nanosheet solution showed a yellow color compared to the colorless undoped titania (Ti_{0.87}O₂) nanosheet solution (Figure S1b). On the basis of the UV-visible absorption spectra, the doped Fe atoms at positive charge state (Fe^{III}) significantly enhanced the absorption in the 300–400 nm range. The absorbance in this range can indicate the Fe^{III} concentration in the nanosheets and, therefore, examine the function of HI acid to remove active metal ions from 2D oxide nanosheets.

Composition Changes of Ti_{0.6}Fe_{0.4}O₂ Nanosheet after HI Acid Treatment. To synthesize the perforated Ti_{0.6}Fe_{0.4}O₂ nanosheet, we progressively introduced the pristine Ti_{0.6}Fe_{0.4}O₂ nanosheets solution into HI acid (Figure 1a). The formation of purple iodine (I₂) molecules on the Ti_{0.6}Fe_{0.4}O₂ nanosheets (I₂-Ti_{0.6}Fe_{0.4}O₂) was easily identified with the naked eye (Figure S2a) and has been confirmed by X-ray photoelectron spectroscopy (XPS) characterization (Figure S2b). The nanosheets were then washed in hot ethanol at 50 °C, removing the as-formed I₂ on the surface and cutting nanopores into the Ti_{0.6}Fe_{0.4}O₂ below to form perforated Ti_{0.6}Fe_{0.4}O₂ nanosheets (H-Ti_{0.6}Fe_{0.4}O₂). Finally, the solution was centrifuged again, and the deposits were dispersed into the tetrabutylammonium hydroxide (TBAOH) solution for further characterization.

Different HI acid concentrations ranging from $C = 0.03$ to 3 mol/L were tested to optimize the formation of the nanopores. The H-Ti_{0.6}Fe_{0.4}O₂ water solution showed a gradual color fading as the HI acid concentration increased, starting from the yellow color of the solution at $C = 0$ to become colorless above

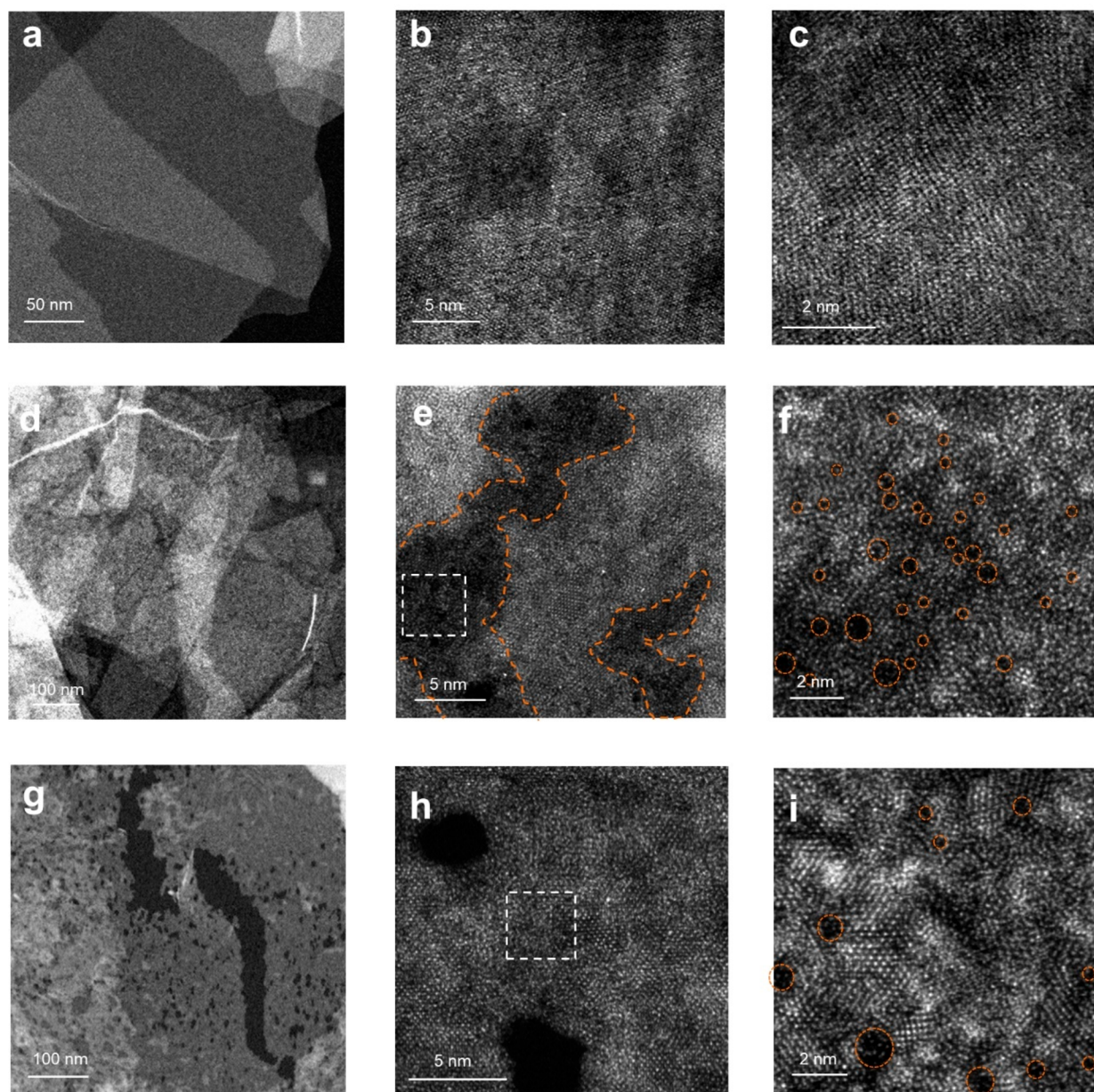


Figure 2. TEM and HRTEM images for $\text{Ti}_{0.6}\text{Fe}_{0.4}\text{O}_2$ before and after the pore creation process. (a–c) Original $\text{Ti}_{0.6}\text{Fe}_{0.4}\text{O}_2$ nanosheets. (d–f) $\text{H-Ti}_{0.6}\text{Fe}_{0.4}\text{O}_2$ obtained after 0.3 mol/L HI acid treatment, where (f) is the magnified image of the dash square in (e). The orange dash trace enclosed area in (e) is the HI acid etched region, and the small orange circles in (f) are the pores in this region. (g–i) $\text{H-Ti}_{0.6}\text{Fe}_{0.4}\text{O}_2$ obtained after 1.2 mol/L HI acid treatment, where (i) is the magnified image of the dash square in (h) and the small orange circles in (i) are the pores in this region.

$C = 0.3$ mol/L (Figure S2c). The UV–visible spectrum shows two peaks at ~ 320 nm and ~ 260 nm, whose intensities $I_{320\text{ nm}}$ and $I_{260\text{ nm}}$ correspond to the concentration of Fe^{III} to Ti^{IV} atoms, respectively (Figure S3). In Figure 1b, the absorbance ratio $I_{320\text{ nm}}/I_{260\text{ nm}}$ decreases from 0.46 for the solution without acid to a minimum value of 0.24 after HI acid treatment at 1.2 mol/L. The $I_{320\text{ nm}}/I_{260\text{ nm}}$ ratio decrease indicates the removal of Fe^{III} atoms from the oxide nanosheets, thus explaining the color fading. Inductive coupled plasma (ICP) was further used to confirm this result and showed that the Fe to Ti ($n_{\text{Fe}}/n_{\text{Ti}}$) ratio decreased from 0.59 to 0.26 (Figure 1c). All these results demonstrated that the Fe^{III} are much more easily removed than Ti^{IV} from the framework. However, after the treatment with concentrated HI acid (3 mol/L), the value of $n_{\text{Fe}}/n_{\text{Ti}}$ increased to 0.39, which is

attributed to the total dissolution of nanosheets by highly concentrated HI acid (3 mol/L). Therefore, these results demonstrated the prior removal of Fe^{III} to Ti^{IV} from the $\text{Ti}_{0.6}\text{Fe}_{0.4}\text{O}_2$ nanosheets at a suitable HI acid concentration.

Structural Change of $\text{Ti}_{0.6}\text{Fe}_{0.4}\text{O}_2$ Nanosheet after HI Acid Treatment. Atomic force microscopy (AFM) and transmission electron microscopy (TEM) were used to characterize the structural changes induced by the pore creation process in the $\text{Ti}_{0.6}\text{Fe}_{0.4}\text{O}_2$ nanosheets before and after HI acid treatment. AFM results (Figure S4) show that HI acid treatment does not impact the thickness or size of the nanosheets, although wrinkles appear when a high concentration of acid is applied. It indicates that the removal of Fe^{III} from the nanosheets preserves the monolayer structure. TEM was used to characterize the microstructural change on

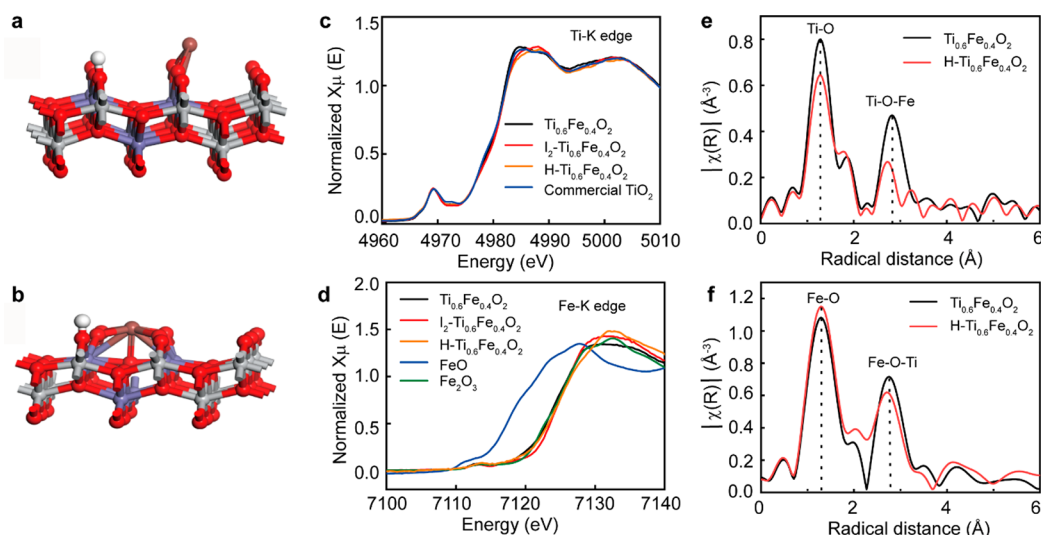


Figure 3. Selective etching mechanism study of $\text{Ti}_{0.6}\text{Fe}_{0.4}\text{O}_2$ by HI acid. (a, b) Structure models of I^- and H^+ ions adsorbed on the (a) TiO_2 -rich region and (b) FeO_2 -rich region. The gray, purple, red, brown, and white spheres represent Ti, Fe, O, I, and H atoms. (c, d) XANES results of Ti K edge and Fe K edge for $\text{Ti}_{0.6}\text{Fe}_{0.4}\text{O}_2$, $\text{I}_2\text{-Ti}_{0.6}\text{Fe}_{0.4}\text{O}_2$, and $\text{H-Ti}_{0.6}\text{Fe}_{0.4}\text{O}_2$ treated in 0.3 mol/L HI acid. (e, f) The k^3 -weighted Fourier transform spectra from EXAFS to see bond difference between original $\text{Ti}_{0.6}\text{Fe}_{0.4}\text{O}_2$ and $\text{H-Ti}_{0.6}\text{Fe}_{0.4}\text{O}_2$.

the in-plane structure. The $\text{H-Ti}_{0.6}\text{Fe}_{0.4}\text{O}_2$ obtained by low concentration (0.1 mol/L) acid treatment showed similar sheet morphology and crystal structure to the original $\text{Ti}_{0.6}\text{Fe}_{0.4}\text{O}_2$ with the atoms arranged in a rectangular unit cell (Figures 2a–c and S5). A few lattice vacancies are visible in both nanosheets, which were certainly formed during the synthetic process of the layered bulk precursors and the protonation process.³¹ According to the elemental mapping on the microscopic area of the original $\text{Ti}_{0.6}\text{Fe}_{0.4}\text{O}_2$, Fe atoms were homogeneously distributed on the whole titania nanosheets (Figure S6). The $n_{\text{Fe}}/n_{\text{Ti}}$ at this area was 0.53, close to the global result obtained by ICP (0.59).

For the $\text{H-Ti}_{0.6}\text{Fe}_{0.4}\text{O}_2$ obtained after 0.3 mol/L HI acid treatment, although the sheet morphology has been preserved, densely distributed nanopores were found on each nanosheet (Figure 2d). The high-resolution TEM image displays two distinct regions on the nanosheets (Figure 2e), i.e., irregular regions with dense subnanopores (dash brown traced region) and regular regions with vacancies. In the dense pore region, the pore size was generally <1 nm with an area density of $\sim 3.3 \times 10^5 \mu\text{m}^{-2}$ (Figure 2f). The size of the pores was much smaller, and the area density of the pores was much higher than other reported perforated 2D materials.^{22,25} The EDS mapping of a microscopic area showed the atomic ratio $n_{\text{Fe}}/n_{\text{Ti}}$ was around 0.2 (Figure S7), much lower than the result (0.53) for the original nanosheets (Figure S6). The drop in the $n_{\text{Fe}}/n_{\text{Ti}}$ ratio is direct evidence of the selective removal of Fe atoms from the nanosheets to create nanopores.

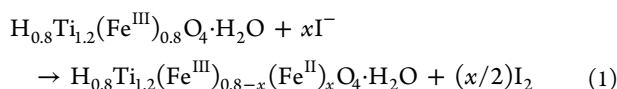
When the acid concentration increased to 1.2 mol L^{-1} , we found that the as-obtained $\text{H-Ti}_{0.6}\text{Fe}_{0.4}\text{O}_2$ still showed a sheet morphology (Figures 2g and S8). But the average size of the pores increased to 4 nm (Figure 2h), and the pore density decreased to $\sim 0.9 \times 10^4 \mu\text{m}^{-2}$. The region far away from the pores also had an irregular structure with a few subnanopores inside (Figure 2i). The semiquantitative EDS analysis by TEM indicated that the atomic ratio $n_{\text{Fe}}/n_{\text{Ti}}$ was further decreased to 0.14 with the increase of acid concentration to 1.2 mol L^{-1} , which originated from the increased size of pores (Figure S9). For the highest acid concentration of 3 mol/L, the sheet

structure became creased with large pores (Figure S10), and the as-obtained $\text{H-Ti}_{0.6}\text{Fe}_{0.4}\text{O}_2$ solution was almost transparent (Figure S2c). These results indicate that the nanosheets were not stable at the highest concentration HI acid (3 mol/L), and most of them were dissolved during the HI acid treatment process. These TEM results demonstrated the selective removal of Fe atoms from the $\text{Ti}_{0.6}\text{Fe}_{0.4}\text{O}_2$ nanosheet, which led to the formation of nanopores whose size and density can be tuned by the concentration of HI acid.

Pore Formation Mechanism. To elucidate the reaction process of the selective removal of Fe atoms from $\text{Ti}_{0.6}\text{Fe}_{0.4}\text{O}_2$ nanosheets, we conducted a reference experiment with pure titania nanosheets and performed DFT calculations. When pure titania nanosheets were treated with HI acid, the purple I_2 remained mostly in solution without attaching to the $\text{Ti}_{0.87}\text{O}_2$ nanosheets. The size of the I_2 particles was also much smaller than that formed on the $\text{Ti}_{0.6}\text{Fe}_{0.4}\text{O}_2$ nanosheets. These differences indicated the unlikely bonding of I_2 on pure titania nanosheets and highlighted the selective bonding with Fe atoms. According to our experiments and previous reports, HI acid could reduce small amounts of TBAOH in the $\text{Ti}_{0.87}\text{O}_2$ solution.²⁸ Therefore, the as-formed I_2 in the $\text{Ti}_{0.87}\text{O}_2$ nanosheet solution was due to the reduction of TBAOH. When we added the original $\text{Ti}_{0.6}\text{Fe}_{0.4}\text{O}_2$ nanosheets into KI solution, the dark red color of the solution due to I^- was not changed, and the purple I_2 sediments did not form. This result indicates the necessity of protons (H^+) for the formation of I_2 .

In the HI acid reduction mechanism, protons activated the oxygen-containing units, and I^- reduced the carbon or metal atoms.^{27,28} According to the Hubbard-corrected density functional theory (DFT+U) calculations, H^+ and I^- ions are favorably adsorbed at both the FeO_2 -rich region ($E_{\text{adsorption}} = -9.43 \text{ eV}$) and TiO_2 -rich region ($E_{\text{adsorption}} = -3.03 \text{ eV}$) of the $\text{Ti}_{0.6}\text{Fe}_{0.4}\text{O}_2$ nanosheets (Figure 3a,b). The I^- ions interact with four neighboring 2-fold coordinated surface O atoms at the FeO_2 -rich region, which leads to a substantial surface relaxation in this region of the oxide nanosheet. We expect the H^+ to be adsorbed at an undercoordinated surface O atom, and

the charge transferred from I^- will reduce Fe^{III} to form Fe^{II} . The following equation can describe the reaction:



Previous work indicated that the divalent (II) charge state metal ions, i.e., Zn^{II} and Mg^{II} , were easily leached out and dissolved by acids.⁴⁴ Therefore, the removed Fe atoms from the nanosheets should be due to the reaction in eq 1.

The ICP result for $I_2-Ti_{0.6}Fe_{0.4}O_2$ obtained in 1.2 mol/L HI acid showed that the n_{Fe}/n_{Ti} ratio was 0.50, close to the value for the original $Ti_{0.6}Fe_{0.4}O_2$ (0.59) but much larger than the value for $H-Ti_{0.6}Fe_{0.4}O_2$ (0.26). Therefore, the reduced Fe^{II} remained in the $I_2-Ti_{0.6}Fe_{0.4}O_2$ and not immediately dissolved into the solution. DFT results indicated that I_2 exhibited strong adsorption energy ($E_{adsorption}$) for -1.51 eV and -1.95 eV in the TiO_2 and FeO_2 regions, respectively (Figure S11). Consequently, on the basis of eq 1, the as-formed I_2 was anchored on the $Ti_{0.6}Fe_{0.4}O_2$ surface, which impeded the immediate dissolution of Fe^{II} into the solution. X-ray photoemission spectroscopic (XPS) and X-ray absorption near edge structure (XANES) results showed that the Fe^{II} ions quickly bonded to oxygen in the solution to form ultrasmall Fe_2O_3 particles covered by the I_2 molecules. High-resolution XPS scans of Ti 2p and Fe 2p³ in $I_2-Ti_{0.6}Fe_{0.4}O_2$ revealed that the peaks for Ti^{IV} and Fe^{III} shifted to higher energy due to the I_2 on the surface (Figure S12). The XANES results of the Ti K and Fe K edges also confirmed that the Ti and Fe atoms in $Ti_{0.6}Fe_{0.4}O_2$ and $I_2-Ti_{0.6}Fe_{0.4}O_2$ only displayed Ti^{IV} and Fe^{III} charge states and that no Fe^{II} existed (Figure 3c,d). Therefore, the Fe_2O_3 particles may be covered by the I_2 molecules and removed together during the ethanol washing process. Compared with the original $Ti_{0.6}Fe_{0.4}O_2$, the bond length for Fe–O–Ti/Ti–O–Fe in the $H-Ti_{0.6}Fe_{0.4}O_2$ nanosheets has slightly changed due to the removal of FeO_2 units from the framework, which may explain the irregular regions in the $H-Ti_{0.6}Fe_{0.4}O_2$ nanosheets (Figure 3e,f).

Pore Structure Regulation Mechanism. DFT calculations were used to simulate the evolution of various defects on $Ti_{0.6}Fe_{0.4}O_2$. We found that the removal of Fe atoms in the form of FeO_2 units from the nanosheets coincided well with the experimental results. We identified two types of stable distributions for the Fe species in the titania nanosheets (Figure S13): *homogeneous* and *island* distribution models. As the number of removed FeO_2 units increases in the homogeneously distributed regions (Figure 4), we observed the formation of vacancies, nanopores, and amorphous structures on the $Ti_{0.6}Fe_{0.4}O_2$. After creating up to two FeO_2 vacancies on the surface of a 3×3 $Ti_{0.6}Fe_{0.4}O_2$ unit cell (with theoretical ratio $n_{Fe}/n_{Ti} = 0.46-0.54$), the original lepidocrocite-like structure was well preserved in the system (Figure 4a,b). This system is close to the structures obtained with <0.1 mol/L HI acid-treated samples (Figures 2a–c and S5). Increasing the number of FeO_2 vacancies in the atomistic model to three yields a theoretical ratio $n_{Fe}/n_{Ti} = 0.36$ (Figure 4c), which is close to the experimental value by ICP (0.33) in the $H-Ti_{0.6}Fe_{0.4}O_2$ obtained after 0.3 mol/L HI acid treatment. The DFT results indicated the formation of a small hole from the absence of Fe and O atoms, which coincided with the microstructures in Figure 2f, where many nanopores were observed. When four FeO_2 units were removed (theoretical $n_{Fe}/n_{Ti} = 0.28$), the large concentration

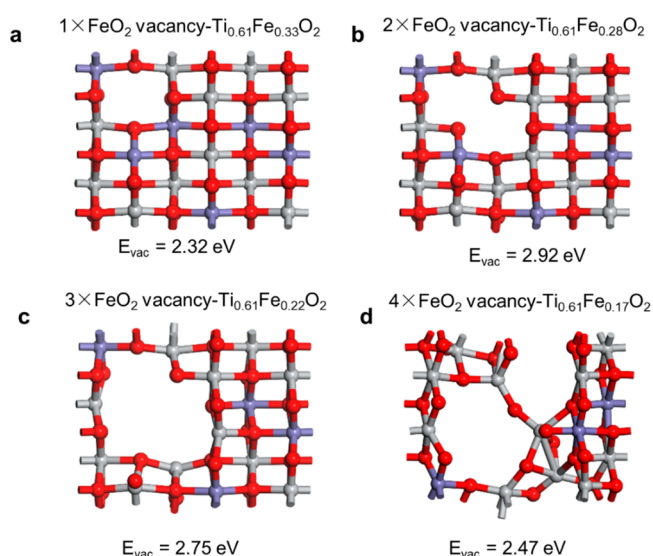


Figure 4. Structural evolution of $Ti_{0.6}Fe_{0.4}O_2$ in the Fe homogeneous distribution model after removing different numbers of FeO_2 units. The vacancy formation energies are presented under the figures. (a) One FeO_2 unit removed from the $Ti_{0.6}Fe_{0.4}O_2$ to form $Ti_{0.61}Fe_{0.33}O_2$. (b) Two FeO_2 units removed from the $Ti_{0.6}Fe_{0.4}O_2$ to form $Ti_{0.61}Fe_{0.28}O_2$. (c) Three FeO_2 units removed from the $Ti_{0.6}Fe_{0.4}O_2$ to form $Ti_{0.61}Fe_{0.22}O_2$. (d) Four FeO_2 units removed from the $Ti_{0.6}Fe_{0.4}O_2$ to form $Ti_{0.61}Fe_{0.17}O_2$.

of vacancies introduced substantial distortions in the $Ti_{0.61}Fe_{0.17}O_2$ nanosheet. The n_{Fe}/n_{Ti} ratio was close to the lowest experimental ICP value of 0.26 in Figure 1c, which was obtained with the 1.2 mol/L HI acid treatment. At this ratio, the relaxed DFT structure formed a highly disordered $H-Ti_{0.6}Fe_{0.4}O_2$ in which amorphous-like domains surrounded some nanopores. This simulated structure was in agreement with the experimental results presented in Figure 2h,i. When the number of vacancies increased to five, the 2D slab became unstable and was completely dissolved.

On the other hand, when the FeO_2 vacancies were formed in the *island* distribution model (Figure S14), the vacancy formation energy was in a range between 1.6 and 2.3 eV, which is lower (e.g., more energetically favored) than in the homogeneous distribution model (2.3–2.9 eV). The *island* model exhibits better structural stability than the *homogeneous* one, so it would not be dissolved even after removing five FeO_2 units from the DFT supercell. This increased stability supported the existence of a creased $H-Ti_{0.6}Fe_{0.4}O_2$ observed experimentally after 3 mol/L HI acid treatment (Figure S10). The simulated results (Figures 4 and S14) confirm the proposed evolution of the selective removal of FeO_2 units from the $Ti_{0.6}Fe_{0.4}O_2$ nanosheets as a function of the HI concentration indicated in Figure 2.

Universality Study of the Pore Creation Method. We also treated the $Ti_{0.6}Fe_{0.4}O_2$ nanosheets with other acids, i.e., hydrochloride (HCl) acid and hydrobromide (HBr) acid, to assess their ability to create defects on the oxide nanosheets. The UV–visible absorption spectra and DFT calculation of the $Ti_{0.6}Fe_{0.4}O_2$ indicated no significant change after treating the two acids at different concentrations (Figures S15 and S16). These results show that these two acids cannot remove FeO_2 units from the $Ti_{0.6}Fe_{0.4}O_2$ and are therefore unsuitable for creating nanopores.

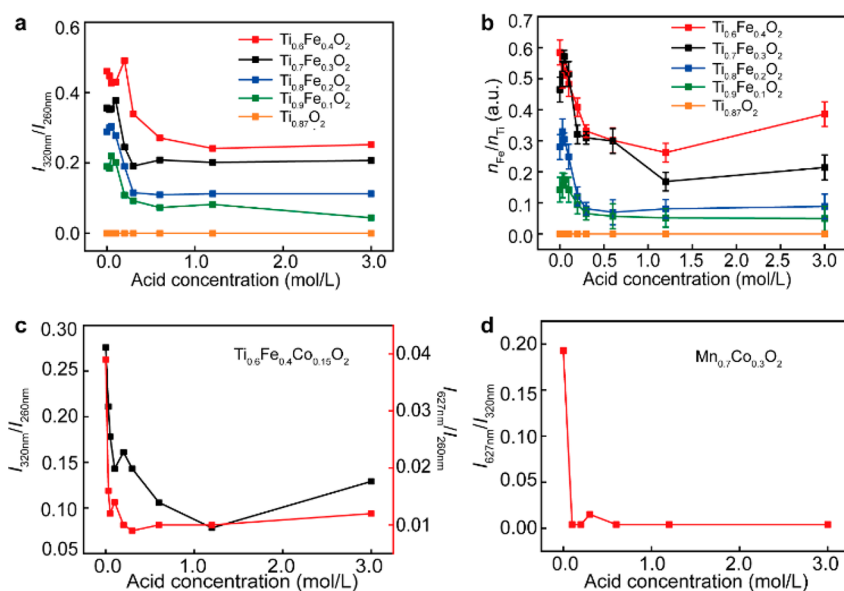


Figure 5. UV–visible absorption spectra and ICP results for other types of oxide nanosheets after the HI acid treatment. (a, b) Evolution of the absorbance and ICP results in the $\text{Ti}_{1-x}\text{Fe}_x\text{O}_2$ ($x = 0, 0.1, 0.2, 0.3, 0.4$) after the HI acid treatment at different concentration. (c, d) Absorbance ratio of Fe^{III} (320 nm), Co^{III} (627 nm) to Ti^{IV} (260 nm) in $\text{Ti}_{0.75}\text{Fe}_{0.10}\text{Co}_{0.15}\text{O}_2$ and Co^{III} (627 nm) to Mn^{IV} (360 nm) in $\text{Mn}_{0.7}\text{Co}_{0.3}\text{O}_2$.

Then, we used different $n_{\text{Ti}}/n_{\text{Fe}}$ ratios to synthesize $\text{Ti}_{1-x}\text{Fe}_x\text{O}_2$ ($x = 0, 0.1, 0.2, 0.3, 0.4$) and treated them with HI acid to assess the tunability of the as-fabricated H– $\text{Ti}_{1-x}\text{Fe}_x\text{O}_2$. The UV–visible absorption spectra of all the treated samples show a drop of absorbance in the 300–400 nm range, corresponding to the selective removal of Fe elements (Figure S17). Therefore, the HI acid treatment successfully creates defects in $\text{Ti}_{1-x}\text{Fe}_x\text{O}_2$ with Fe atoms inside. Interestingly, the increase of Fe in the original $\text{Ti}_{1-x}\text{Fe}_x\text{O}_2$ yields the highest value of $I_{320\text{nm}}/I_{260\text{nm}}$ after the HI acid treatment (Figure 5a), indicating that more Fe atoms remain in the H– $\text{Ti}_{1-x}\text{Fe}_x\text{O}_2$ nanosheets if more Fe atoms are present in the original nanosheet. This conclusion has been further confirmed by the ICP results (Figure 5b), which showed the same change tendency of $n_{\text{Ti}}/n_{\text{Fe}}$ as the UV–visible spectroscopic results for all the samples. The large tunability of composition and defects number/size of the as-obtained H– $\text{Ti}_{1-x}\text{Fe}_x\text{O}_2$ may give them wide application potentials in different fields.

The universality of this method on other types of 2D oxides has been demonstrated by the selective etching of Fe/Co in $\text{Ti}_{0.75}\text{Fe}_{0.10}\text{Co}_{0.15}\text{O}_2$ and Mn/Co in the $\text{Mn}_{0.7}\text{Co}_{0.3}\text{O}_2$ nanosheets with HI acid treatment (Figures 5c,d and S18). In the $\text{Ti}_{0.75}\text{Fe}_{0.10}\text{Co}_{0.15}\text{O}_2$, after normalization by the absorbance of the Ti^{IV} at ~ 260 nm, the absorbance of Co^{III} at ~ 627 nm rapidly decreased even after 0.03 mol/L HI acid treatment and then showed a minor increase with the acid concentration. However, the concentration of Fe^{III} gradually decreased as the acid concentration increased, indicating that the stability sequence was as follows: TiO_2 unit > FeO_2 unit > CoO_2 unit. In the case of $\text{Mn}_{0.7}\text{Co}_{0.3}\text{O}_2$, both Mn and Co were dissolved by the HI acid. After normalization by the absorbance of Mn^{IV} at 360 nm, the absorbance of Co^{III} at ~ 627 nm rapidly decreased up to 0.1 mol/L HI acid treatment, which suggests that CoO_2 units were removed before the MnO_2 unit from the reaction kinetics. All these results demonstrated the successful selective removal of active metal atoms, such as Fe, Co, Mn, from oxide nanosheets by HI acid.

To give a more generic principle for this selective removal process, we use the standard electrode potential of ions (vs RHE).⁴⁵ The standard electrode potential for the I_2/I^- , Cl_2/Cl^- , Br_2/Br^- , $\text{Fe}^{3+}/\text{Fe}^{2+}$, $\text{Ti}^{4+}/\text{Ti}^{3+}$, $\text{Co}^{3+}/\text{Co}^{2+}$, $\text{Mn}^{4+}/\text{Mn}^{2+}$ was 0.54 V, 1.36 V, 1.09 V, 0.77 V, 0.1 V, 1.83 V, 1.22 V, respectively. It means the oxidation potential is ordered as follows: $\text{Co}^{3+} > \text{Cl}_2 > \text{Mn}^{4+} > \text{Br}_2 > \text{Fe}^{3+} > \text{I}_2 > \text{Ti}^{4+}$, and the reduction potential is the reverse, i.e., $\text{Co}^{2+} < \text{Cl}^- < \text{Mn}^{2+} < \text{Br}^- < \text{Fe}^{2+} < \text{I}^- < \text{Ti}^{3+}$. Therefore, HI acid cannot reduce Ti^{4+} to Ti^{3+} but can thermodynamically reduce Co^{3+} , Mn^{4+} , and Fe^{3+} into divalent charges. Therefore, the oxidation potential of molecules/ions larger than I_2 , such as Ni^{IV} , Co^{III} , Mn^{IV} , Al^{III} , Cu^{II} , etc.³⁰ will be removed from the oxide nanosheets, while ions with stronger reduction potential than I^- , such as Ti^{IV} , Sn^{IV} , Ta^{V} , and Nb^{V} , will be stable in the framework.

Assembly Behavior of Perforated Oxide Nanosheets and Their Application for Water Purification. The H– $\text{Ti}_{0.6}\text{Fe}_{0.4}\text{O}_2$ obtained by using different concentrations of HI acid was assembled into films by vacuum filtration to understand the influence of these holes on the assembly behavior and intrinsic properties of oxides nanosheets. Interestingly, we found that the layer spacing decreased from the original 1.6 nm to ~ 0.9 nm after the acid treatment (Figure 6a). It is known from the AFM results that the nanosheets showed unchanged thickness after the acid treatment (Figure S4). According to previous reports, each layer of trapped water molecules in the original sheets film increased the layer spacing by 0.3–0.35 nm.³¹ Therefore, the reduced layer spacing after HI acid treatment was due to the removal of bilayer water molecules from the assembled films. During the vacuum filtration process, the water molecules escape easily through the nanopores in the H– $\text{Ti}_{0.6}\text{Fe}_{0.4}\text{O}_2$ nanosheet, while they are trapped in the original $\text{Ti}_{0.6}\text{Fe}_{0.4}\text{O}_2$ film. On the other hand, the intensity of the d -spacing peak for the films has dramatically reduced after the acid treatment, even for those treated at low acid concentration, similar to the KOH-activated rGO films.²² This result indicated that the quality of the layered structure of H– $\text{Ti}_{0.6}\text{Fe}_{0.4}\text{O}_2$ film was much poorer than the original

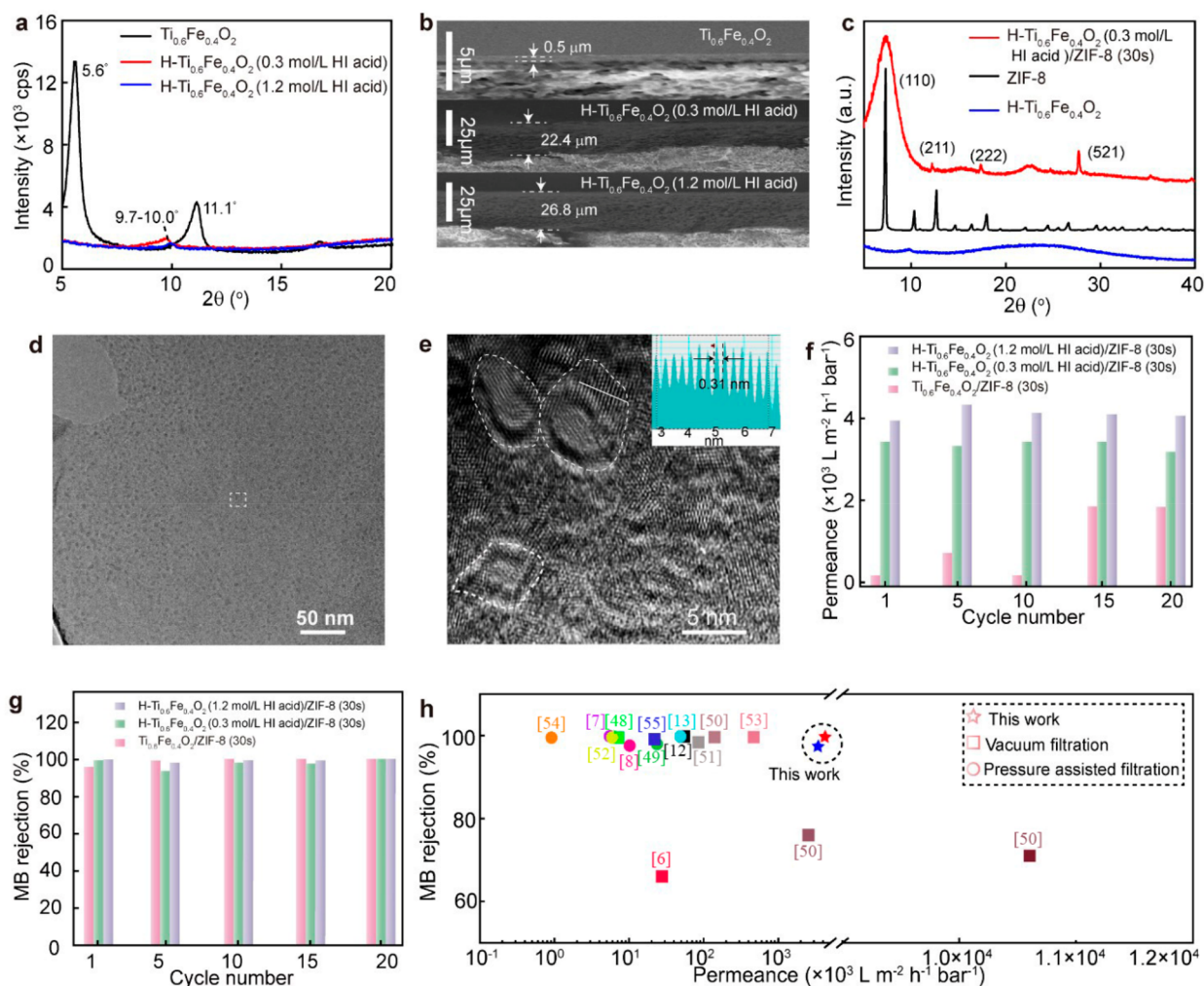


Figure 6. Assembly behavior of perforated oxide nanosheets and their application for water purification. (a, b) XRD patterns and SEM images of the as-fabricated films from $\text{Ti}_{0.6}\text{Fe}_{0.4}\text{O}_2$ and $\text{H-Ti}_{0.6}\text{Fe}_{0.4}\text{O}_2$ obtained by treating with different concentrations of HI acid. (c) XRD patterns of the $\text{H-Ti}_{0.6}\text{Fe}_{0.4}\text{O}_2$, ZIF-8, and $\text{H-Ti}_{0.6}\text{Fe}_{0.4}\text{O}_2/\text{ZIF-8}$, where the $\text{H-Ti}_{0.6}\text{Fe}_{0.4}\text{O}_2$ was obtained by 0.3 mol/L HI acid treatment. (d, e) TEM, and HRTEM images of the $\text{H-Ti}_{0.6}\text{Fe}_{0.4}\text{O}_2/\text{ZIF-8}$, showing the ultrasmall ZIF-8 particles (3–5 nm) densely grown in the pores of $\text{H-Ti}_{0.6}\text{Fe}_{0.4}\text{O}_2$. (f, g) Water permeance and MB rejection of the ZIF-8 grown nanosheet films after different cycles. (h) Comparison of MB rejection and water permeance of $\text{H-Ti}_{0.6}\text{Fe}_{0.4}\text{O}_2/\text{ZIF-8}$ with other 2D material-based membranes reported in the literature.^{6–8,12,13,48–55} The data details can be found in Table S1.

$\text{Ti}_{0.6}\text{Fe}_{0.4}\text{O}_2$ film, which was confirmed by the cross-section SEM images (Figure 6b). The as-formed defects, such as nanopores and irregularly arranged regions on the original $\text{Ti}_{0.6}\text{Fe}_{0.4}\text{O}_2$ nanosheets, reduced the van der Waals force between the layers, allowing more randomness in the spacing between layers in $\text{H-Ti}_{0.6}\text{Fe}_{0.4}\text{O}_2$ films. The thickness of the $\text{H-Ti}_{0.6}\text{Fe}_{0.4}\text{O}_2$ film increased to $>20 \mu\text{m}$, which was ~ 40 -fold of the thickness of the original $\text{Ti}_{0.6}\text{Fe}_{0.4}\text{O}_2$ film with the same weight amount ($\sim 0.5 \text{ mg}$). The assembly process by vacuum filtration of the $\text{H-Ti}_{0.6}\text{Fe}_{0.4}\text{O}_2$ films demonstrated a much easier penetration of solvents than the original $\text{Ti}_{0.6}\text{Fe}_{0.4}\text{O}_2$ films.

As a proof of concept for potential applications, we used our films for water purification of organic pollutants. Compared with the original $\text{Ti}_{0.6}\text{Fe}_{0.4}\text{O}_2$ film, the $\text{H-Ti}_{0.6}\text{Fe}_{0.4}\text{O}_2$ films showed much larger water permeance but poorer methylene blue (MB) rejection selectivity (Figure S19). The performance degradation with the cycling process was much faster in the $\text{H-Ti}_{0.6}\text{Fe}_{0.4}\text{O}_2$ films than in the original $\text{Ti}_{0.6}\text{Fe}_{0.4}\text{O}_2$ film. For instance, in the films assembled from $\text{H-Ti}_{0.6}\text{Fe}_{0.4}\text{O}_2$ obtained

by treating with 1.2 mol/L HI acid, namely, $\text{H-Ti}_{0.6}\text{Fe}_{0.4}\text{O}_2$ (1.2 mol/L HI acid), their MB rejection and water permeance decreased to 44% and $700 \text{ L m}^{-2} \text{ h}^{-1} \text{ bar}^{-1}$ after 20 cycles. This is probably because the MB molecules are smaller than the nanopores on the $\text{H-Ti}_{0.6}\text{Fe}_{0.4}\text{O}_2$ and their adsorption in the $\text{H-Ti}_{0.6}\text{Fe}_{0.4}\text{O}_2$ membranes. Initially, the MB molecules are adsorbed in the $\text{H-Ti}_{0.6}\text{Fe}_{0.4}\text{O}_2$ membranes.⁴⁶ As the cycle number increases, the adsorption of the MB molecules in the membrane is saturated. Then, the excessive MB molecules will directly pass through the nanopores, leading to the reduced MB rejection as the cycle number increases. In the meantime, the adsorbed MB molecules also impede the water flow pass through the membranes, leading to the decreased water permeance.

To enhance the MB rejection of $\text{H-Ti}_{0.6}\text{Fe}_{0.4}\text{O}_2$ films for water purification, we grew ZIF-8 nanocrystals inside the nanopores of the $\text{H-Ti}_{0.6}\text{Fe}_{0.4}\text{O}_2$ nanosheets. The ZIF-8 with subnanometer channels may act as steric filters, providing excellent rejection to organic pollutants due to the subnanometer channels and avoiding the blockage of organic

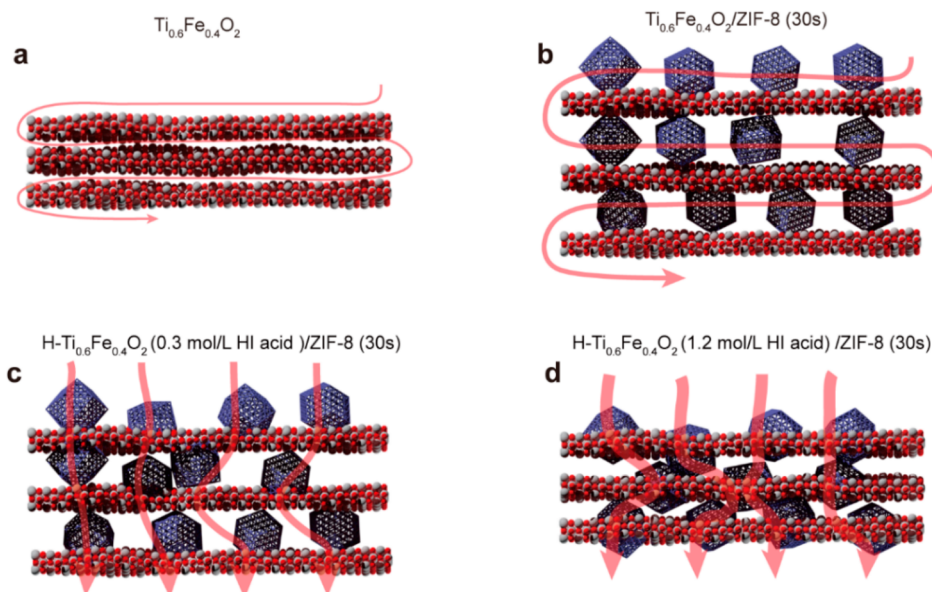


Figure 7. Schematic illustration of the mechanism for the water permeance in different membranes: (a) original $\text{Ti}_{0.6}\text{Fe}_{0.4}\text{O}_2$ membrane; (b) $\text{Ti}_{0.6}\text{Fe}_{0.4}\text{O}_2/\text{ZIF-8}$ (30 s) membrane; (c) $\text{Ti}_{0.6}\text{Fe}_{0.4}\text{O}_2$ (0.3 mol/L HI acid)/ZIF-8 (30 s) membrane; (d) $\text{Ti}_{0.6}\text{Fe}_{0.4}\text{O}_2$ (1.2 mol/L HI acid)/ZIF-8 (30 s) membrane.

pollutants inside the pores.⁴⁷ From the XRD pattern of the hybrid film (Figure 6c), the first peak from ZIF-8 was rather broad. According to the Debye–Scherrer equation, the sizes of ZIF-8 grown on the $\text{H-Ti}_{0.6}\text{Fe}_{0.4}\text{O}_2$ (0.3 mol/L HI acid) were 2.9 nm. The peak positions have also shifted to lower positions than the pure ZIF-8 crystals, which indicated strain in the ZIF-8 particles. In Figure 6d,e, the TEM image on the surface of the $\text{H-Ti}_{0.6}\text{Fe}_{0.4}\text{O}_2$ (0.3 mol/L HI acid)/ZIF-8 indicated that the ZIF-8 particles nucleated at the edge of the nanopores and blocked them. The HRTEM image showed that the particles have clear crystal fringes of 0.31 nm, corresponding to the (521) crystal plane of ZIF-8 on the $\text{H-Ti}_{0.6}\text{Fe}_{0.4}\text{O}_2$ (0.3 mol/L HI acid). Different ZIF-8 nanocrystals growth times were tested from 30 s to 5 min (Figure S20). All the as-fabricated films showed >97% MB rejection with good cycling stability. Among them, the hybrid film with the shortest ZIF-8 growth time (30 s) showed the highest water permeance around $3390 \text{ L m}^{-2} \text{ h}^{-1} \text{ bar}^{-1}$, indicating that the excessive ZIF-8 on the surface reduced the water permeance through the film.

To optimize the water permeance through the hybrid film, we also *in situ* grew ZIF-8 nanocrystals for 30 s on $\text{Ti}_{0.6}\text{Fe}_{0.4}\text{O}_2$ and $\text{H-Ti}_{0.6}\text{Fe}_{0.4}\text{O}_2$ (0.3 mol/L HI acid). The $\text{H-Ti}_{0.6}\text{Fe}_{0.4}\text{O}_2$ (1.2 mol/L) showed stable water permeance of $4260 \text{ L m}^{-2} \text{ h}^{-1} \text{ bar}^{-1}$ with 99.3% MB rejection (Figure 6f,g). This rejection rate is better than the literature reported 2D materials-based membranes with >90% MB rejection, and the water permeance of $\text{H-Ti}_{0.6}\text{Fe}_{0.4}\text{O}_2$ (1.2 mol/L HI acid)/ZIF-8 films is 1–3 orders of magnitude higher (Figure 6h and Table S1).^{6–8,12,13,48–55}

The superior water permeance of this hybrid film is ascribed to the dominance of its configuration in the following aspects (Figure 7a–d): (1) ZIF-8 nanocrystals impede the restacking of the mesoporous film under transmembrane pressure and provide much more water flow pathways in the film directions (Figure 7a,b); (2) ZIF-8 nanocrystals increase capillary forces of the film and promote the water absorption (Figure 7b);¹³ (3) the mesoporous structure of $\text{H-Ti}_{0.6}\text{Fe}_{0.4}\text{O}_2$ film increases water permeance through the whole film (Figure 6b); (4) the

pores on the nanosheets provide much more water flow pathways through the vertical direction of the film. So we can conclude that for larger pores, one would generally obtain higher water permeance (Figure 7c,d). The excellent performance for $\text{H-Ti}_{0.6}\text{Fe}_{0.4}\text{O}_2/\text{ZIF-8}$, i.e., excellent pollutants rejection and large water permeance, clearly demonstrated the potential of the perforated oxide nanosheets for real water purification applications. Noteworthy, these perforated oxide nanosheets are ceramic materials, which may be used in more severe conditions, such as high temperature and high pressure, than organic polymer membranes.⁵⁶

CONCLUSION

A method has been developed to create nanopores in high area density on unilamellar bi/trimetallic oxide nanosheets using HI acid. During the synthetic process, the H^+ and I^- interacted with the $\text{Ti}_{0.6}\text{Fe}_{0.4}\text{O}_2$ nanosheet, where I^- transferred the electron to Fe^{III} , reducing it to be Fe^{II} and forming I_2 molecules. The Fe^{II} was not stable and oxidized into Fe_2O_3 particles, covered by the as-formed I_2 molecules on the nanosheet surface. After washing the I_2 molecules with hot methanol, the Fe_2O_3 particles were selectively removed from the nanosheets, leading to the formation of nanopores on the nanosheets. The size and area density of the pores can be tuned by the reaction kinetics by controlling the HI acid concentration. The universality of this method was experimentally demonstrated in the $\text{Ti}_{1-x}\text{Fe}_x\text{O}_2$ ($x = 0.1–0.4$), $\text{Ti}_{0.75}\text{Fe}_{0.1}\text{Co}_{0.15}\text{O}_2$, and $\text{Mn}_{0.7}\text{Co}_{0.3}\text{O}_2$. A more generic principle from the electrode potential has been proposed, where metal ions, such as Fe^{III} , Co^{III} , Ni^{III} , Mn^{IV} , and Al^{III} , with a higher electrode potential than the I^- could also be reduced and removed from the host nanomaterials by HI acid. As an application, the perforated $\text{Ti}_{0.6}\text{Fe}_{0.4}\text{O}_2$ has been used to grow ultrasmall ZIF-8 particles inside the pores for water purification, which showed excellent MB rejection (99.3%) and large water permeance ($4260 \text{ L m}^{-2} \text{ h}^{-1} \text{ bar}^{-1}$) with good cycling stability. The large water permeance was related to the ZIF-8 particles and mainly ascribed to the mesoporous

structure of assembled H–Ti_{0.6}Fe_{0.4}O₂ film and the high-density nanopores on the nanosheets. The perforated 2D oxides fabricated in this work may also show great potential in technological fields related to small size ions/molecules, such as separators for Li–S batteries and gas separation. Finally, the developed selective etching strategy may be used to synthesize various porous/perforated nanomaterials with fine microstructures.

■ ASSOCIATED CONTENT

SI Supporting Information

The Supporting Information is available free of charge at <https://pubs.acs.org/doi/10.1021/acsami.2c01474>.

Description of computational methods and DFT calculations; atomistic structure of Ti_{0.6}Fe_{0.4}O₂ nanosheets; models of molecular and ionic adsorption on Ti_{0.6}Fe_{0.4}O₂; atomistic models of defects in Ti_{0.6}Fe_{0.4}O₂ nanosheets; AFM and UV–visible absorption spectra of the original Ti_{0.6}Fe_{0.4}O₂ nanosheet; optical, TEM, and HRTEM images of H–Ti_{0.6}Fe_{0.4}O₂; UV–visible absorption spectra of the Ti_{0.6}Fe_{0.4}O₂ solutions after different HI acid treatments; EDS mapping from HRTEM, HAADF, and TEM images of H–Ti_{0.6}Fe_{0.4}O₂ samples; structures of molecular I₂ adsorbed at Ti_{0.6}Fe_{0.4}O₂; XPS analysis for Ti_{0.6}Fe_{0.4}O₂ and I₂–Ti_{0.6}Fe_{0.4}O₂; Fe distribution models in the Ti_{0.6}Fe_{0.4}O₂; structural evolution of FeO₂-defective Ti_{0.6}Fe_{0.4}O₂; UV–visible absorption spectra of the H–Ti_{0.6}Fe_{0.4}O₂ treated by HCl and HBr acids; DFT models of ionic adsorption on the nanosheets; UV–visible absorption spectra of the H–Ti_{1-x}Fe_xO₂ treated by different concentrations of HI acid; methylene blue rejection and water permeance of the as-fabricated and ZIF-8 containing films (PDF)

■ AUTHOR INFORMATION

Corresponding Author

Xingke Cai – *Institute for Advanced Study, Shenzhen University, Shenzhen 518060, P. R. China*; orcid.org/0000-0003-3878-4456; Email: cai.xingke@szu.edu.cn

Authors

Yongtao Li – *Institute for Advanced Study, Shenzhen University, Shenzhen 518060, P. R. China*

José Julio Gutiérrez Moreno – *Institute for Advanced Study, Shenzhen University, Shenzhen 518060, P. R. China*; Present Address: Barcelona Supercomputing Center (BSC), C/Jordi Girona 31, 08034 Barcelona, Spain; orcid.org/0000-0002-1564-9879

Zhaoqi Song – *Institute for Advanced Study, Shenzhen University, Shenzhen 518060, P. R. China*

Dongqing Liu – *College of Mechatronics and Control Engineering, Shenzhen University, Shenzhen 518060, China*

Maoyu Wang – *School of Chemical, Biological, and Environmental Engineering, Oregon State University, Corvallis, Oregon 97331, United States*

Aymeric Ramiere – *College of Physics and Optoelectronic Engineering, Shenzhen University, Shenzhen 518060, China*; orcid.org/0000-0002-9283-404X

Zhenxing Feng – *School of Chemical, Biological, and Environmental Engineering, Oregon State University, Corvallis, Oregon 97331, United States*; orcid.org/0000-0001-7598-5076

Qingshan Jason Niu – *Institute for Advanced Study, Shenzhen University, Shenzhen 518060, P. R. China*; orcid.org/0000-0003-0129-1236

Takayoshi Sasaki – *International Center for Materials Nanoarchitectonics, National Institute for Materials Science, Tsukuba, Ibaraki 305-0044, Japan*; orcid.org/0000-0002-2872-0427

Complete contact information is available at: <https://pubs.acs.org/doi/10.1021/acsami.2c01474>

Author Contributions

#Y.L. and J.J.G.M. contributed equally to the manuscript. X.C. played a decisive role in raising the idea of the research and completed the manuscript writing and revision. Y.L. conducted the research and carried out the data analysis. J.J.G.M. carried out the theoretical simulations. Z.S., D.L., M.W., A.R., Z.F., Q.J.N., and T.S. carried out part of the data analysis. All authors assisted in writing and revising the manuscript. All authors read and approved the final manuscript.

Notes

The authors declare no competing financial interest.

■ ACKNOWLEDGMENTS

X.C. acknowledges the funding from Natural Science Foundation of China (Grant 52003163), Science and Technology Innovation Commission of Shenzhen (Grants KQTD20170810105439418 and 20200812112006001), and Shenzhen University-Taipei University of Science and Technology Collaboration Project (Grants 2022005 and 2022015). He also appreciates the help from electron microscopy center in Shenzhen University for the testing of the aberration corrected HAADF STEM. Z.F. thanks the support from U.S. National Science Foundation under Grant No. CBET-1949870 and DMR-1832803. The XAS measurements were done at beamline 9-BM of the Advanced Photon Source, which is a U.S. Department of Energy (DOE) Office of Science User Facility operated for the DOE Office of Science by Argonne National Laboratory under Contract DE-AC02-06CH11357. Q.J.N. acknowledges the funding support from Key Project of National Natural Science Foundation of China (Grant U2006230). This work was partly supported by the World Premier International Research Center Initiative on Materials Nanoarchitectonics (WPI-MANA), MEXT, Japan, and CREST of the Japan Science and Technology Agency (JST). T.S. acknowledges the support from JSPS KAKENHI (Grant 15H02004). J.J.G.M. acknowledges the financial funding from the Postdoctoral Science Foundation of China under Grant 2018M643152, the Paratera cloud server, and the National Supercomputing Center in Shenzhen for the provision of computational resources and technical support.

■ REFERENCES

- (1) Survey, U.S.G. One Estimate of Global Water Distribution. <http://water.usgs.gov/edu/gallery/watercyclekids/earth-water-distribution.html> (accessed May 25, 2021).
- (2) Van der Bruggen, B. Sustainable Implementation of Innovative Technologies for Water Purification. *Nat. Rev. Chem.* **2021**, *5* (4), 217–218.
- (3) Zeng, M.; Chen, M.; Huang, D.; Lei, S.; Zhang, X.; Wang, L.; Cheng, Z. Engineered Two-Dimensional Nanomaterials: an Emerging Paradigm for Water Purification and Monitoring. *Mater. Horiz.* **2021**, *8* (3), 758–802.

- (4) Khan, S. T.; Malik, A. Engineered Nanomaterials for Water Decontamination and Purification: From Lab to Products. *J. Hazard. Mater.* **2019**, *363*, 295–308.
- (5) Abraham, J.; Vasu, K. S.; Williams, C. D.; Gopinadhan, K.; Su, Y.; Cherian, C. T.; Dix, J.; Prestat, E.; Haigh, S. J.; Grigorieva, I. V.; Carbone, P.; Geim, A. K.; Nair, R. R. Tunable Sieving of Ions Using Graphene Oxide Membranes. *Nat. Nanotechnol.* **2017**, *12* (6), 546–550.
- (6) Hu, M.; Mi, B. Enabling Graphene Oxide Nanosheets as Water Separation Membranes. *Environ. Sci. Technol.* **2013**, *47* (8), 3715–3723.
- (7) Qiu, Z.; Ji, X.; He, C. Fabrication of a Loose Nanofiltration Candidate From Polyacrylonitrile/Graphene Oxide Hybrid Membrane via Thermally Induced Phase Separation. *J. Hazard. Mater.* **2018**, *360*, 122–131.
- (8) Wang, L.; Wang, N.; Li, J.; Li, J.; Bian, W.; Ji, S. Layer-By-Layer Self-Assembly of Polycation/GO Nanofiltration Membrane with Enhanced Stability and Fouling Resistance. *Sep. Purif. Technol.* **2016**, *160*, 123–131.
- (9) Guan, K.; Zhao, D.; Zhang, M.; Shen, J.; Zhou, G.; Liu, G.; Jin, W. 3D Nanoporous Crystals Enabled 2D Channels in Graphene Membrane with Enhanced Water Purification Performance. *J. Membr. Sci.* **2017**, *542*, 41–51.
- (10) Zhang, M.; Mao, Y.; Liu, G.; Liu, G.; Fan, Y.; Jin, W. Molecular Bridges Stabilize Graphene Oxide Membranes in Water. *Angew. Chem., Int. Ed.* **2020**, *59* (4), 1689–1695.
- (11) Zhang, M.; Guan, K.; Shen, J.; Liu, G.; Fan, Y.; Jin, W. Nanoparticles@Rgo Membrane Enabling Highly Enhanced Water Permeability and Structural Stability with Preserved Selectivity. *AIChE J.* **2017**, *63* (11), 5054–5063.
- (12) Goh, K.; Jiang, W.; Karahan, H. E.; Zhai, S.; Wei, L.; Yu, D.; Fane, A. G.; Wang, R.; Chen, Y. All-Carbon Nanoarchitectures as High-Performance Separation Membranes with Superior Stability. *Adv. Funct. Mater.* **2015**, *25* (47), 7348–7359.
- (13) Zhang, W.-H.; Yin, M.-J.; Zhao, Q.; Jin, C.-G.; Wang, N.; Ji, S.; Ritt, C. L.; Elimelech, M.; An, Q.-F. Graphene Oxide Membranes with Stable Porous Structure for Ultrafast Water Transport. *Nat. Nanotechnol.* **2021**, *16* (3), 337–343.
- (14) Weng, Q.; Kvashnin, D. G.; Wang, X.; Cretu, O.; Yang, Y.; Zhou, M.; Zhang, C.; Tang, D.-M.; Sorokin, P. B.; Bando, Y.; Golberg, D. Tuning of the Optical, Electronic, and Magnetic Properties of Boron Nitride Nanosheets with Oxygen Doping and Functionalization. *Adv. Mater.* **2017**, *29* (28), 1700695.
- (15) Qian, J.; Wu, X.; Cao, Y.; Ai, X.; Yang, H. High Capacity and Rate Capability of Amorphous Phosphorus for Sodium Ion Batteries. *Angew. Chem., Int. Ed.* **2013**, *52* (17), 4633–4636.
- (16) Li, Y.; Jin, R.; Xing, Y.; Li, J.; Song, S.; Liu, X.; Li, M.; Jin, R. Macroscopic Foam-Like Holey Ultrathin g-C₃N₄ Nanosheets for Drastic Improvement of Visible-Light Photocatalytic Activity. *Adv. Energy Mater.* **2016**, *6* (24), 1601273.
- (17) Kotakoski, J.; Krasheninnikov, A.; Kaiser, U.; Meyer, J. From Point Defects in Graphene to Two-Dimensional Amorphous Carbon. *Phys. Rev. Lett.* **2011**, *106* (10), 105505.
- (18) Peng, L.; Xiong, P.; Ma, L.; Yuan, Y.; Zhu, Y.; Chen, D.; Luo, X.; Lu, J.; Amine, K.; Yu, G. Holey Two-Dimensional Transition Metal Oxide Nanosheets for Efficient Energy Storage. *Nat. Commun.* **2017**, *8* (1), 15139.
- (19) Peng, L.; Fang, Z.; Zhu, Y.; Yan, C.; Yu, G. Holey 2D Nanomaterials for Electrochemical Energy Storage. *Adv. Energy Mater.* **2018**, *8* (9), 1702179.
- (20) Tao, Q.; Dahlqvist, M.; Lu, J.; Kota, S.; Meshkian, R.; Halim, J.; Palisaitis, J.; Hultman, L.; Barsoum, M. W.; Persson, P. O.; Rosen, J. Two-Dimensional Mo_{1.33}C Mxene with Divacancy Ordering Prepared from Parent 3D Laminate with In-Plane Chemical Ordering. *Nat. Commun.* **2017**, *8* (1), 14949.
- (21) Mkhoyan, K. A.; Contryman, A. W.; Silcox, J.; Stewart, D. A.; Eda, G.; Mattevi, C.; Miller, S.; Chhowalla, M. Atomic and Electronic Structure of Graphene-Oxide. *Nano Lett.* **2009**, *9* (3), 1058–1063.
- (22) Yin, Y.; Han, J.; Zhang, Y.; Zhang, X.; Xu, P.; Yuan, Q.; Samad, L.; Wang, X.; Wang, Y.; Zhang, Z.; Zhang, P.; Cao, X.; Song, B.; Jin, S. Contributions of Phase, Sulfur Vacancies, and Edges to the Hydrogen Evolution Reaction Catalytic Activity of Porous Molybdenum Disulfide Nanosheets. *J. Am. Chem. Soc.* **2016**, *138* (25), 7965–7972.
- (23) Danda, G.; Drndić, M. Two-Dimensional Nanopores and Nanoporous Membranes for Ion and Molecule Transport. *Curr. Opin. Biotechnol.* **2019**, *55*, 124–133.
- (24) Su, S.; Wang, X.; Xue, J. Nanopores in Two-Dimensional Materials: Accurate Fabrication. *Mater. Horiz.* **2021**, *8* (5), 1390–1408.
- (25) Zhu, Y.; Murali, S.; Stoller, M. D.; Ganesh, K. J.; Cai, W.; Ferreira, P. J.; Pirkle, A.; Wallace, R. M.; Cychosz, K. A.; Thommes, M.; Su, D.; Stach, E. A.; Ruoff, R. S. Carbon-Based Supercapacitors Produced by Activation of Graphene. *Science* **2011**, *332* (6037), 1537–1541.
- (26) Ren, C. E.; Zhao, M.-Q.; Makaryan, T.; Halim, J.; Boota, M.; Kota, S.; Anasori, B.; Barsoum, M. W.; Gogotsi, Y. Porous Two-Dimensional Transition Metal Carbide (MXene) Flakes for High-Performance Li-Ion Storage. *ChemElectroChem* **2016**, *3* (5), 689–693.
- (27) Reusch, W.; LeMahieu, R. A Versatile Ketone Synthesis. The Reduction of α -Diketones and α -Ketols by Hydriodic Acid. *J. Am. Chem. Soc.* **1964**, *86* (15), 3068–3072.
- (28) Konieczny, M.; Harvey, R. G. Efficient Reduction of Polycyclic Quinones, Hydroquinones, and Phenols with Hydriodic Acid. *J. Org. Chem.* **1979**, *44* (26), 4813–4816.
- (29) Moon, I. K.; Lee, J.; Ruoff, R. S.; Lee, H. Reduced Graphene Oxide by Chemical Graphitization. *Nat. Commun.* **2010**, *1*, 73.
- (30) Bratsch, S. G. Standard Electrode Potentials and Temperature Coefficients in Water at 298.15 K. *J. Phys. Chem. Ref. Data* **1989**, *18* (1), 1–21.
- (31) Sasaki, T.; Watanabe, M.; Hashizume, H.; Yamada, H.; Nakazawa, H. Macromolecule-Like Aspects for a Colloidal Suspension of an Exfoliated Titanate. Pairwise Association of Nanosheets and Dynamic Reassembling Process Initiated from it. *J. Am. Chem. Soc.* **1996**, *118* (35), 8329–8335.
- (32) Osada, M.; Yoguchi, S.; Itose, M.; Li, B.-W.; Ebina, Y.; Fukuda, K.; Kotani, Y.; Ono, K.; Ueda, S.; Sasaki, T. Controlled Doping of Semiconducting Titania Nanosheets for Tailored Spinelectronic Materials. *Nanoscale* **2014**, *6* (23), 14227–14236.
- (33) Sakai, N.; Fukuda, K.; Ma, R.; Sasaki, T. Synthesis and Substitution Chemistry of Redox-Active Manganese/Cobalt Oxide Nanosheets. *Chem. Mater.* **2018**, *30* (5), 1517–1523.
- (34) Blöchl, P. E. Projector Augmented-Wave Method. *Phys. Rev. B* **1994**, *50* (24), 17953–17979.
- (35) Kresse, G.; Joubert, D. From Ultrasoft Pseudopotentials to the Projector Augmented-Wave Method. *Phys. Rev. B* **1999**, *59* (3), 1758–1775.
- (36) Perdew, J. P.; Wang, Y. Accurate and Simple Analytic Representation of the Electron-Gas Correlation Energy. *Phys. Rev. B* **1992**, *45* (23), 13244–13249.
- (37) Himmetoglu, B.; Floris, A.; de Gironcoli, S.; Cococcioni, M. Hubbard-Corrected DFT Energy Functionals: The LDA+U Description of Correlated Systems. *Int. J. Quantum Chem.* **2014**, *114* (1), 14–49.
- (38) Gutiérrez Moreno, J. J.; Nolan, M. Ab Initio Study of the Atomic Level Structure of the Rutile TiO₂(110)-Titanium Nitride (TiN) Interface. *ACS Appl. Mater. Interfaces* **2017**, *9* (43), 38089–38100.
- (39) Gutiérrez Moreno, J. J.; Fronzi, M.; Lovera, P.; O’Riordan, A.; Nolan, M. Stability of Adsorbed Water on TiO₂-TiN Interfaces. A First-Principles and Ab Initio Thermodynamics Investigation. *J. Phys. Chem. C* **2018**, *122* (27), 15395–15408.
- (40) Gutiérrez Moreno, J. J.; Fronzi, M.; Lovera, P.; O’Riordan, A.; Ford, M. J.; Li, W.; Nolan, M. Structure, Stability and Water Adsorption on Ultra-Thin TiO₂ Supported on TiN. *Phys. Chem. Chem. Phys.* **2019**, *21* (45), 25344–25361.
- (41) Bo, Z.; Thornburg, N. E.; Peng, L.; Gutiérrez Moreno, J. J.; Nolan, M.; Marks, L. D.; Notestein, J. M. Direct Visualization of

Independent Ta Centers Supported on Two-Dimensional TiO₂ Nanosheets. *Nano Lett.* **2019**, *19* (11), 8103–8108.

(42) Dzade, N. Y.; Roldan, A.; De Leeuw, N. H. A Density Functional Theory Study of the Adsorption of Benzene on Hematite (α -Fe₂O₃) Surfaces. *Minerals* **2014**, *4* (1), 89.

(43) Cai, X.; Ozawa, T. C.; Funatsu, A.; Ma, R.; Ebina, Y.; Sasaki, T. Tuning the Surface Charge of 2D Oxide Nanosheets and the Bulk Scale Production of Superlattice-like Composites. *J. Am. Chem. Soc.* **2015**, *137*, 2844–2847.

(44) Wang, L.; Sasaki, T. Titanium Oxide Nanosheets: Graphene Analogues with Versatile Functionalities. *Chem. Rev.* **2014**, *114*, 9455–9486.

(45) Milazzo, G.; Caroli, S.; Braun, R. D. Tables of Standard Electrode Potentials. *J. Electrochem. Soc.* **1978**, *125* (6), 261C.

(46) Tan, I. A. W.; Ahmad, A. L.; Hameed, B. Adsorption of Basic Dye on High-Surface-Area Activated Carbon Prepared From Coconut Husk: Equilibrium, Kinetic and Thermodynamic Studies. *J. Hazard. Mater.* **2008**, *154*, 337–346.

(47) Ebie, K.; Li, F.; Azuma, Y.; Yuasa, A.; Hagishita, T. Pore Distribution Effect of Activated Carbon in Adsorbing Organic Micropollutants from Natural Water. *Water Res.* **2001**, *35* (1), 167–79.

(48) Zhang, P.; Gong, J.-L.; Zeng, G.-M.; Song, B.; Cao, W.; Liu, H.-Y.; Huan, S.-Y.; Peng, P. Novel “Loose” GO/MoS₂ Composites Membranes with Enhanced Permeability for Effective Salts and Dyes Rejection at Low Pressure. *J. Membr. Sci.* **2019**, *574*, 112–123.

(49) Wang, Q.; Zhao, G.; Li, C.; Meng, H. Orderly Stacked Ultrathin Graphene Oxide Membranes on a Macroporous Tubular Ceramic Substrate. *J. Membr. Sci.* **2019**, *586*, 177–184.

(50) Thebo, K. H.; Qian, X.; Zhang, Q.; Chen, L.; Cheng, H.-M.; Ren, W. Highly Stable Graphene-Oxide-Based Membranes with Superior Permeability. *Nat. Commun.* **2018**, *9* (1), 1486.

(51) Kang, H.; Shi, J.; Liu, L.; Shan, M.; Xu, Z.; Li, N.; Li, J.; Lv, H.; Qian, X.; Zhao, L. Sandwich Morphology and Superior Dye-Removal Performances for Nanofiltration Membranes Self-Assembled via Graphene Oxide and Carbon Nanotubes. *Appl. Surf. Sci.* **2018**, *428*, 990–999.

(52) Huang, L.; Chen, J.; Gao, T.; Zhang, M.; Li, Y.; Dai, L.; Qu, L.; Shi, G. Reduced Graphene Oxide Membranes for Ultrafast Organic Solvent Nanofiltration. *Adv. Mater.* **2016**, *28* (39), 8669–8674.

(53) Wang, W.; Eftekhari, E.; Zhu, G.; Zhang, X.; Yan, Z.; Li, Q. Graphene Oxide Membranes with Tunable Permeability due to Embedded Carbon Dots. *Chem. Commun.* **2014**, *50* (86), 13089–13092.

(54) Wang, N.; Ji, S.; Zhang, G.; Li, J.; Wang, L. Self-Assembly of Graphene Oxide and Polyelectrolyte Complex Nanohybrid Membranes for Nanofiltration and Pervaporation. *Chem. Eng. J.* **2012**, *213*, 318–329.

(55) Han, Y.; Xu, Z.; Gao, C. Ultrathin Graphene Nanofiltration Membrane for Water Purification. *Adv. Funct. Mater.* **2013**, *23* (29), 3693–3700.

(56) Sada, Y.; Yoshioka, T.; Nakagawa, K.; Shintani, T.; Iesako, R.; Kamio, E.; Matsuyama, H. Preparation and Characterization of Organic Chelate Ligand (OCL)-Templated TiO₂-ZrO₂ Nanofiltration Membranes. *J. Membr. Sci.* **2019**, *591*, 117304.

Recommended by ACS

Concave ZnFe₂O₄ Hollow Octahedral Nanocages Derived from Fe-Doped MOF-5 for High-Performance Acetone Sensing at Low-Energy Consumption

Xue-Zhi Song, Xiao-Feng Wang, *et al.*

NOVEMBER 02, 2017
INORGANIC CHEMISTRY

READ 

Quaternary Ammonium-Mediated Delamination of Europium-Based Metal–Organic Framework into Ultrathin Nanosheets for the Selective Photoelectro...

Jiaqiang Liu, Dan Li, *et al.*

DECEMBER 02, 2021
INORGANIC CHEMISTRY

READ 

Two-Dimensional Zeolitic Imidazolate Framework-L-Derived Iron–Cobalt Oxide Nanoparticle-Composed Nanosheet Array for Water Oxidation

Yinge Li, Jianlong Wang, *et al.*

APRIL 22, 2019
INORGANIC CHEMISTRY

READ 

Co-MOF Nanosheets Etched by FeCl₂ Solution for Enhanced Electrocatalytic Oxygen Evolution

Weijun Zhang, Lihui Zhou, *et al.*

APRIL 11, 2022
ENERGY & FUELS

READ 

Get More Suggestions >